(I) Corrected scattering and reabsorption effects of canopy SIF based on SCOPE

1、theoretical basis

T**he spectral invariant theory with a spectral invariant $\boldsymbol{\rho}$** (recollisional probability) **and bidirectional gap fraction** has been successfully used to better understand the absorption and scattering effects within the canopy (Stenberg et al., 2016). **However, it assumed that the canopy is bounded underneath by a non-reflecting surface (the 'black-soil' conditions).** Based on the above assumptions and the similar scattering processes for SIF photons and reflected photons, the SIF escape probability from leaf level to canopy level in observing direction Ω can be expressed as:

$$\varepsilon_{CL}(\lambda,\Omega) = \frac{BRF(\lambda,\Omega)}{i_0\omega_L(\lambda)} \quad \text{(S1)}$$

Where ε_{CL} indicates the canopy escape efficiency from leaf to canopy, λ is the spectrum band, Ω is the observational angle. BRF is the bi-directional reflectance, i_0 is the canopy interception probability, and ω_L is the leaf albedo.

In addition, the escape probability for SIF from the PS level to the leaf level ($\varepsilon_{LP}(\lambda)$) is closely related to the leaf chlorophyll content but wavelength dependent (Gitelson et al., 1998; Porcar-Castell et al., 2014). Consequently, the SIF escape probability from the PS level to the canopy level can be expressed as:

$$\varepsilon_{CP}(\lambda,\Omega) = \varepsilon_{LP}(\lambda) \times \varepsilon_{CL}(\lambda) = \varepsilon_{LP}(\lambda) \times \frac{BRF(\lambda,\Omega)}{i_0\omega_L(\lambda)} \quad \text{(S2)}$$

The $\omega_L(\lambda)$ is not easy to be accurately measured, and the $\varepsilon_{LP}(\lambda)$ cannot also be approximately estimated with absence of chlorophyll content.

Calculating i_0 requires additional knowledge of canopy architecture, including the leaf projection function ($G(\theta)$, Ross, 1981), leaf area index (LAI), solar zenith angle (SZA, θ), and the clumping index (CI; Chen, 1996). While both $G(\theta)$, LAI, and CI

are measurable quantities, both strongly vary in time and space, making them difficult to quantify remotely (Ryu et al., 2010). Based on the simplifying assumption that i_0 is approximated by the fraction of absorbed photosynthetically active radiation (fPAR) (Gates et al., 1965; Zeng et al., 2019). The SCOPE simulations were used to validate the close relationship between $fPAR$ and i_0 (Figure S1).

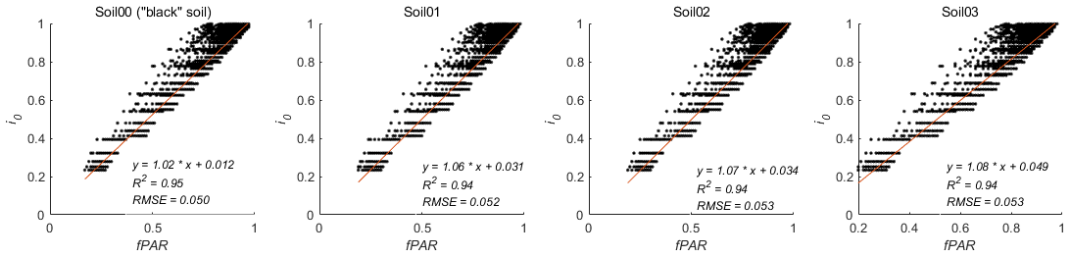

Figure S1. $fPAR$ is a good approximation of canopy directional interceptions, i_0. All values generated using SCOPE (Table S1) for different soil background (Figure S2). "Black" soil with reflectance of 0 named as Soil00, field measured soil reflectance with three levels of brightness named as Soil01, Soil02, and Soil03.

2、Simulated dataset based on SCOPE

In this study, we used **SCOPE v1.73 version**. The amount of absorption of SIF by leaves is mainly related to **chlorophyll content** (Agati et al., 1998), while the canopy scattering is mainly related to the canopy structure parameters (LAI) and solar-view geometries (SZA). Therefore, we parameterized SCOPE for sets of different leaf chlorophyll contents (Cab), LAI levels, and different SZAs.Values or sources of some important input parameters required for SCOPE model are listed in **Table S1**. The viewing zenith angle was set as 25° (the tower-based observation angle). Leaf angle distribution is assumed to be spherical, which is a good approximation in crops such as corn (Lemeur and Blad, 1974; Verhoef and Bach, 2007).

In addition, we also evaluated the effects of **different soil backgrounds** (Figure S2; "Black" soil with reflectance of 0 named as Soil00, field measured soil reflectance with three levels of brightness named as Soil01, Soil02, and Soil03) on the performance

of the f_{esc}_688 calculated by $\frac{Red_v}{fPAR}$. For each soil background, TOC reflectance, TOC SIF, and total SIF emission of the 48000 scenarios were simulated.

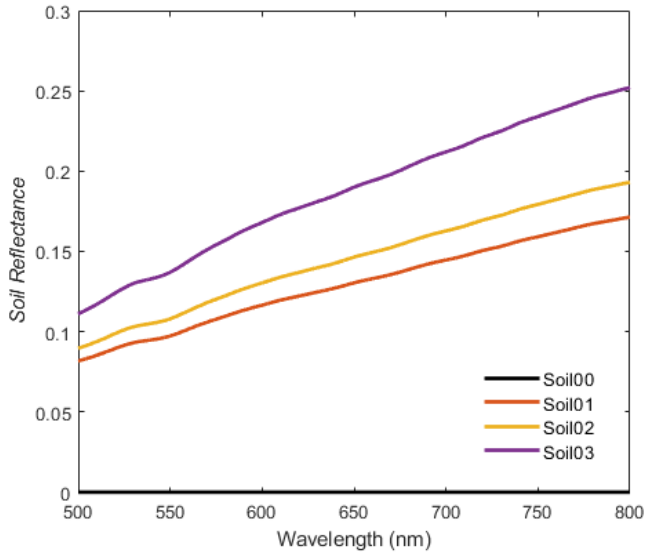

Figure S2. Different soil reflectance used in SCOPE simulation.

Table S1. The main input parameters of the SCOPE model simulations for each soil background (Soil01, Soil02, Soil03, Soil04)

Parameters	Symbols	Units	Range
Chlorophyll $a + b$ content	C_{ab}	$\mu g\ cm^{-2}$	2-80
Leaf area index	LAI	$m^2\ m^{-2}$	0.5-6
Solar zenith angle	tts	°	20-60; 55-90
Incoming shortwave radiation (0.4-2.5μm)	Rin	$W\ m^{-2}$	50-500

3、Uncertainties of $fPAR$ estimated by WDRVI

In addition, we used SCOPE to validate the performance of $fPAR$ estimated by WDRVI (Figures S3 and S4). From the results, we can see that WDRVI is a good proxy of $fPAR$ for different soil backgrounds. However, **it should be noted that WDRVI can not reflect the impact of direct and diffuse radiation components on $fPAR$, and it will bring some uncertainties to this study.**

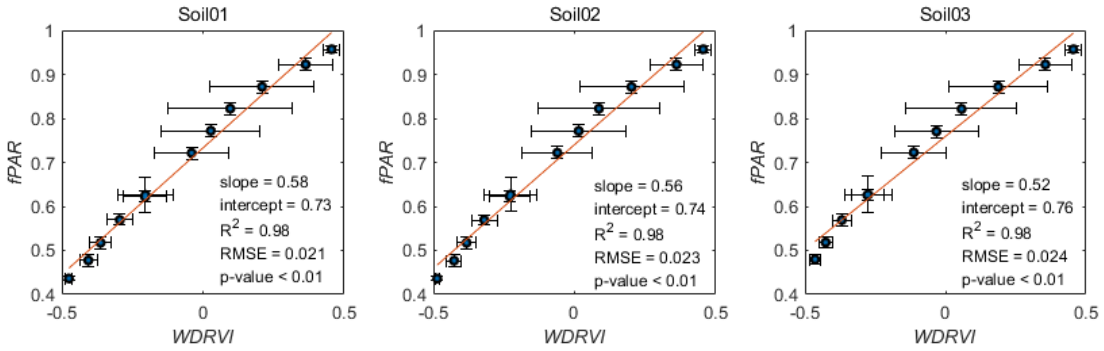

Figure S3. The wide dynamic range vegetation index (WDRVI) is a good approximation of the fraction of absorbed photosynthetically active radiation, $fPAR$. The data were averaged at an interval of 0.1. All values generated using SCOPE model simulations for canopies with different leaf area indices, leaf chlorophyll contents and solar zenith angles (**20-60°**).

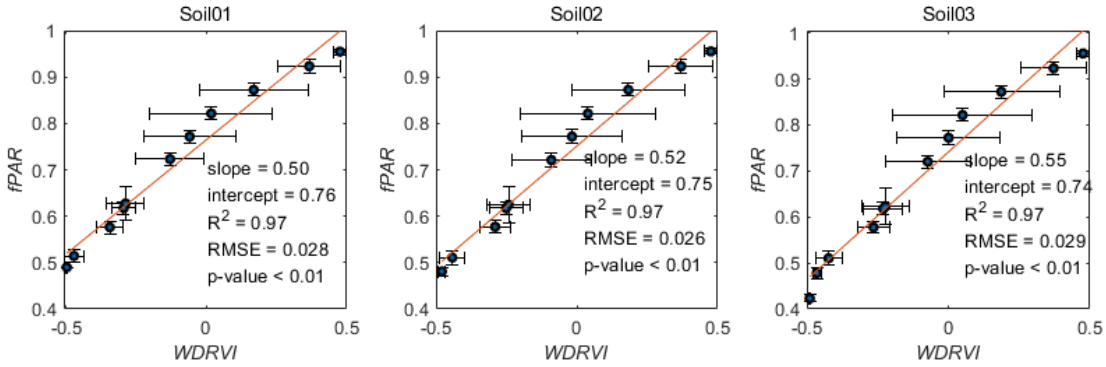

Figure S4. The wide dynamic range vegetation index (WDRVI) is a good approximation of the fraction of absorbed photosynthetically active radiation, $fPAR$. The data were averaged at an interval of 0.1. All values generated using SCOPE model simulations for canopies with different leaf area indices, leaf chlorophyll contents and solar zenith angles (**55-90°**).

Although the coefficients (0.516 and 0.726) were derived empirically from another work (Liu et al., 2019), we found that the coefficients (Table S2) obtained from SCOPE simulations agreed well with that and showed no significant difference for different solar zenith angles.

Table S2. Fitted coefficients based on SCOPE simulations

Datasets	Soil background	Coefficient a	Coefficient b	Significance
Solar zenith angles (20-60°)	Soil01	0.58	0.73	p-value = 0.26 (>0.05) for coefficient a; p-value = 0.56 (>0.05) for coefficient b
	Soil02	0.56	0.74	
	Soil03	0.52	0.76	
Solar zenith angles (55-90°)	Soil01	0.50	0.76	
	Soil02	0.52	0.75	
	Soil03	0.55	0.74	

4、Evaluation of the corrected method using PROSPECT-D and SCOPE：

In this study, we used PROSPECT-D leaf model to evaluate the effects of leaf biochemical parameters on ω_L. Detailed parameters used in PROSPECT-D can be found in Table S3.

Table S3. The main input parameters of the PROSPECT-D model simulations

Parameters	units	Value or range
N（Leaf structural parameter）		1.0-1.6; step 0.2
LCC（Leaf chlorophyll content）	$\mu g\ cm^{-2}$	10-80; step 10
C_{ar}（Leaf carotenoid content）	$\mu g\ cm^{-2}$	25%LCC
C_w（Equivalent thickness）	cm	0.0015
C_m（Dry matter content）	$g\ cm^{-2}$	0.005 - 0.02; step 0.005
C_{Ant}（Leaf anthocyanin content）	$\mu g\ cm^{-2}$	1
C_{brown}（Leaf brown pigment content）		0 - 0.3; step 0.1

From Figure S5, we can see that ω_{688} and ω_{760} showed different sensitivities in response to LCC. ω_{688} was more sensitive to chlorophyll content and showed a nonlinear response curve (Figure S5a). This phenomenon can be explained by the increase of chlorophyll concentration would lead to the absorbed radiation per unit chlorophyll molecule decrease (Porcar-Castell et al., 2014). In addition, ω_{688} was less sensitive to Cm, N, and Cbrown.

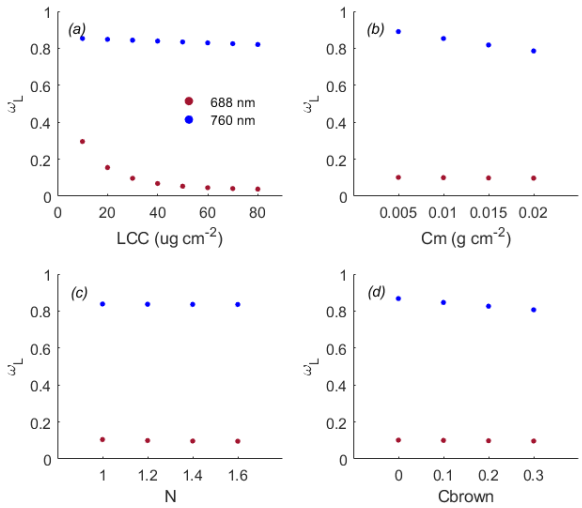

Figure S5. Sensitivities of ω_L to LCC (a), Cm (b), N (c) and Cbrown (d) in ted band (688 nm, the red scatters) and far-red band (760 nm, the blue scatters)

Based on the results shown in Figure S5, we used the fitted curve in Figure S5a and put it into the SCOPE simulations. From Figure S6, f_{esc_688} and Φ_{F_688} estimated by $\frac{Red_v}{fPAR}$ agreed well with that in SCOPE. However, it should be noted that f_{esc_688} and Φ_{F_688} exhibited a nonlinear response to Cab, which indicated that chlorophyll content largely affected the estimation of f_{esc_688} and Φ_{F_688}. Therefore, it would bring some uncertainties for studying the temperature responses of Φ_{F_688} without carefully considering the influences of variations in chlorophyll content during growth periods.

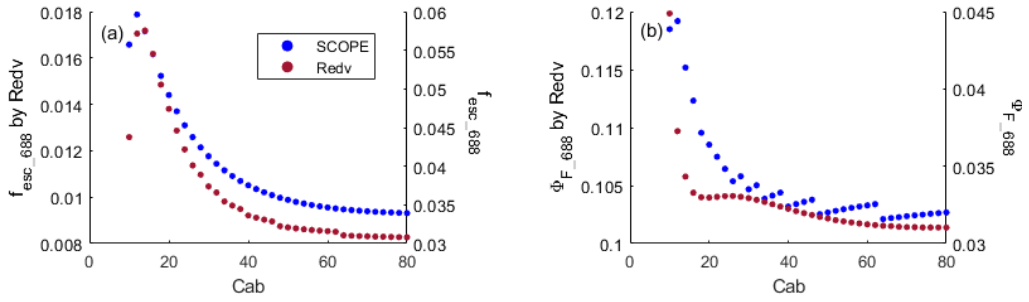

Figure S6. Comparison of f_{esc_688} estimated by $\frac{Red_v}{fPAR}$ (red scatters) and f_{esc_688} of SCOPE (blue scatters) in relationship with Cab (a), and the corresponding Φ_{F_688} in response to Cab (b).

In addition, we also evaluated the performance of the total red SIF calculated by the canopy red SIF divided by the $\frac{Red_v}{fPAR}$, and compared to the total red SIF based on SCOPE (Figures S7 and S8). From the results, we can see that $tSIF_{688}$ estimated by $\frac{Red_v}{fPAR}$ shows a good relationship with $tSIF_{688}$ based on SCOPE. **However, it should be noted that NDVI^2 brings a nonlinear effect on the evaluation of $tSIF_{688}$ despite its role in reducing the impacts of soil background. In this study, we can see that $fPAR$ did not show obvious changes during overwintering period, which indicated that chlorophyll content changed a little (Figure 5g). Therefore, our results were reliable to some degree (Figure S9).**

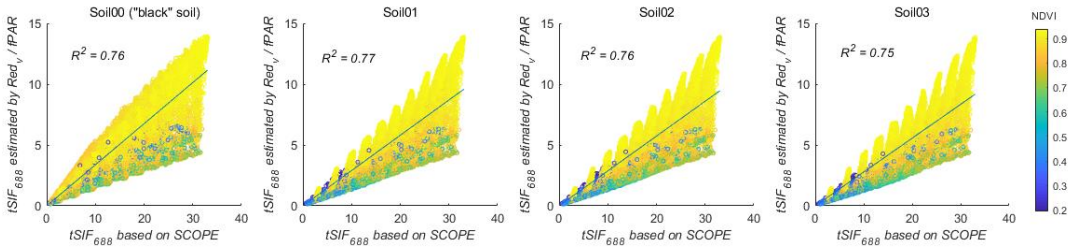

Figure S7. The relationships of $tSIF_{688}$ estimated by $\frac{Red_v}{fPAR}$ and based on SCOPE for different soil background and for canopies with different leaf area indices, leaf chlorophyll contents and solar zenith angles (**20-60°**).

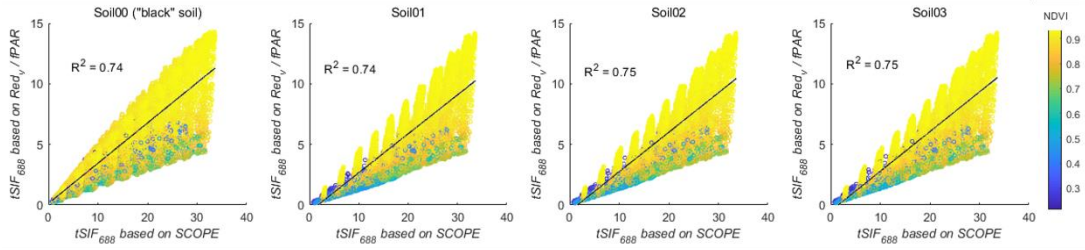

Figure S8. The relationships of $tSIF_{688}$ estimated by $\frac{Red_v}{fPAR}$ and based on SCOPE for different soil background and for canopies with different leaf area indices, leaf chlorophyll contents and solar zenith angles (**55-90°**).

5、Comparison of $\frac{Red_v}{fPAR}$ and random forest (RF) in this study:

From Figure 4f and Figure S9, we can see that no matter $\frac{Red_v}{fPAR}$ or RF exhibited **a similar trend**. It also demonstrates our results have certain degree of credibility.

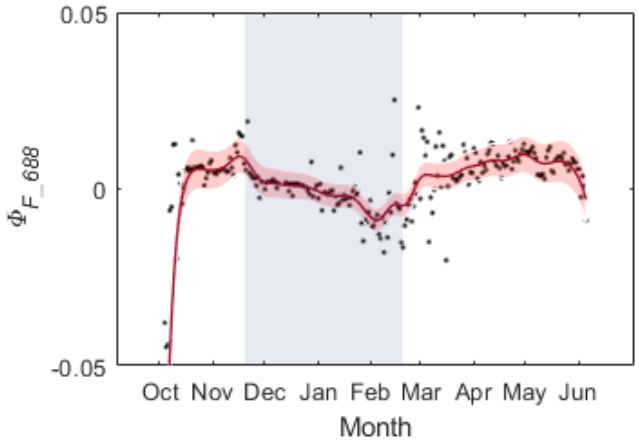

Figure S9. Seasonal changes of Φ_{F_688} estimated by random forest (RF) based on Liu et al. (2019)

(II) Times series of other variables and their relationships with T_a

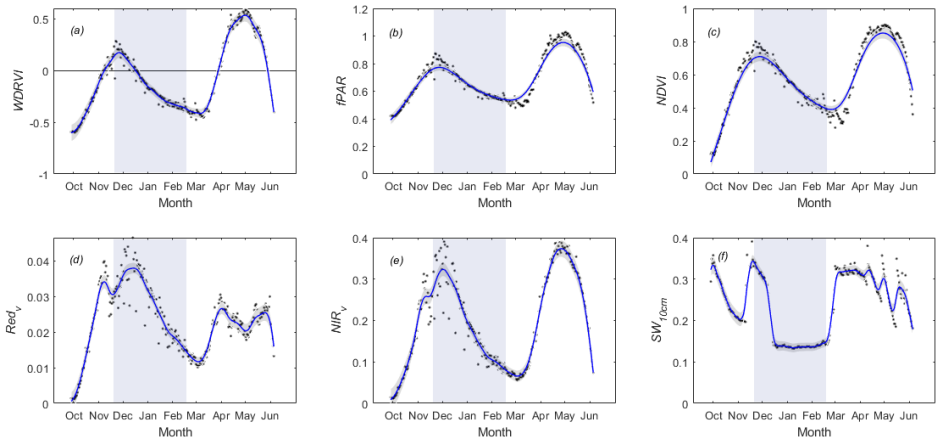

Figure S10. Seasonal dynamics of daily mean WDRVI (a), $fPAR$ (b), NDVI (c), Red_v (d), NIR_v (e), and the soil water content at 10 cm (SW_{10cm}, f). The blue shaded rectangle represents the overwintering periods. Local regression was used to smooth the data. The black shaded area indicates the 95% confidence interval.

(III) The effects of clear and cloudy weather conditions on the SIF-GPP relationship by considering T_a

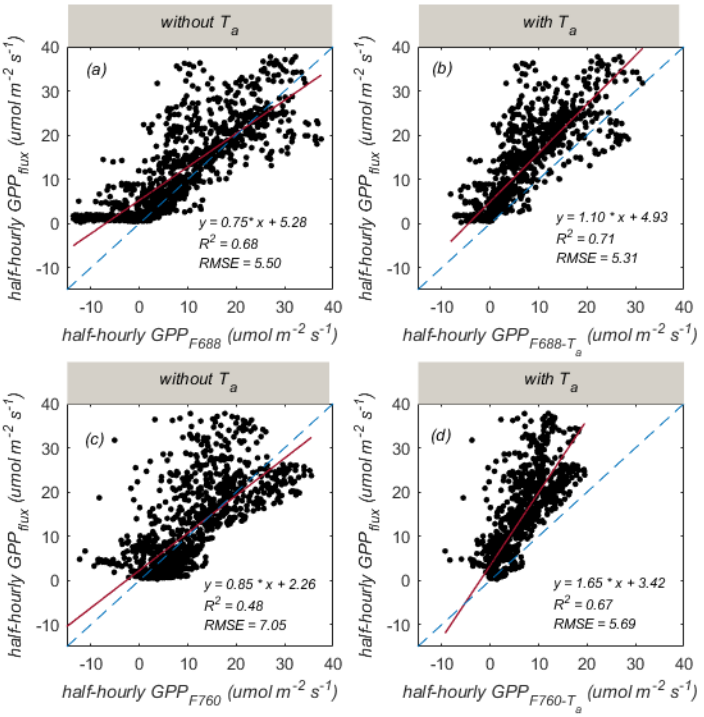

Figure S11. The relationships of GPP with $tSIF_{688}$ (a), $tSIF_{688} * f(Ta)$ (b), $tSIF_{760}$ (c), and $tSIF_{760} * f(T_a)$ (d) based on half-hour measurements on the sunny days. The blue dotted line is the 1:1 line.

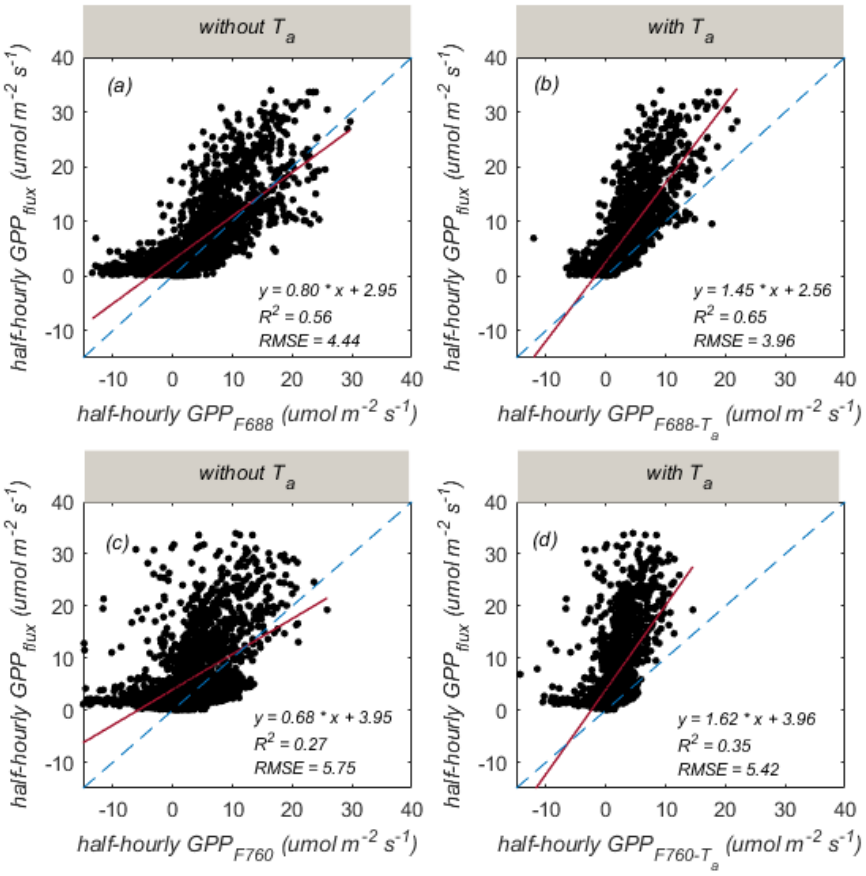

Figure S12. The relationships of GPP with $tSIF_{688}$ (a), $tSIF_{688} * f(Ta)$ (b), $tSIF_{760}$ (c), and $tSIF_{760} * f(T_a)$ (d) based on half-hour measurements on the cloudy days. The blue dotted line is the 1:1 line.

(IV) The changes in canopy structure during overwintering periods.

The canopy structure can be viewed through field camera. However, the camera was set up since summer of 2021. Therefore, we can infer the canopy structure over the overwintering period between 2020 and 2021 from that over the overwintering period between 2021 and 2022.

Figure S13. Changes of canopy structure during overwintering periods between 2021 and 2022.

(V) The ANCOVA analysis of red SIF quantum yield and far-red SIF quantum yield at leaf and photosystem level

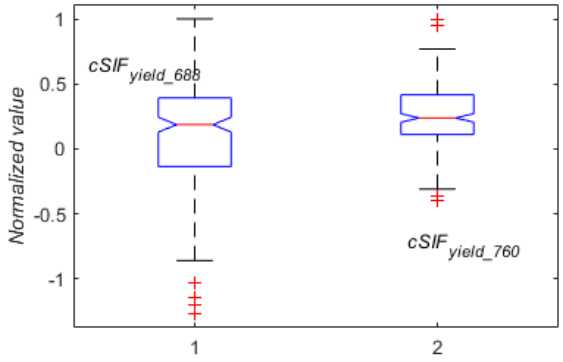

Figure S14. The results of ANCOVA analysis of $cSIF_{yield\_688}$ and $cSIF_{yield\_760}$ based on daily mean data.

Table S4. The ANCOVA table for $cSIF_{yield\_688}$ and $cSIF_{yield\_760}$

Source	SS	df	MS	F	Prob>F
Columns	2.4792	1	2.47922	21.42	4.914e-06
Error	48.841	422	0.11574		
Total	51.3202	423			

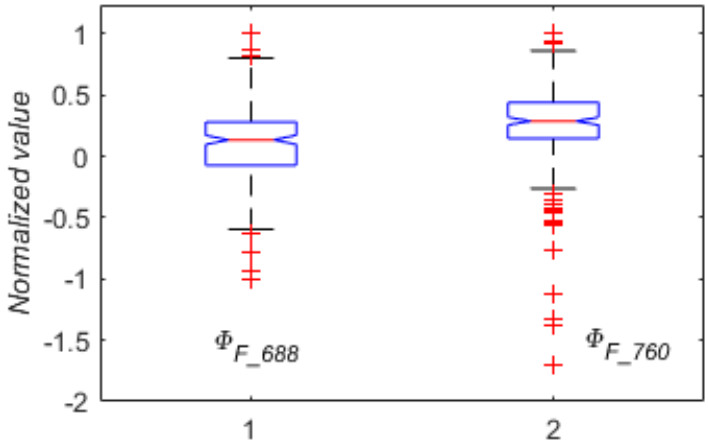

Figure S15. The results of ANCOVA analysis of Φ_{F_686} and Φ_{F_760} based on daily mean data.

Table S5. The ANCOVA table for Φ_{F_686} and Φ_{F_760}

Source	SS	df	MS	F	Prob>F
Columns	0.996	1	0.99962	5.47	0.02
Error	77.165	422	0.18286		
Total	78.1648	423			

(VI) An equivalent improvement in SIF-based GPP estimation if omitted the negative $tSIF$ values.

Because photosynthesis and fluorescence responded differently to temperature (Figure 8), we further explored the $tSIF$-GPP relationship by considering the influence of temperature. By using the empirical temperature-corrected equation, the GPP estimation based on $tSIF_{760}$ was improved (RMSE dropped from 6.34 to 5.56 $umol\ CO_2\ m^{-2}\ s^{-1}$, while R2 values increased from 0.47 to 0.59; Figure S16d). Similar results can also be seen from the $tSIF_{688}$-GPP relationship by considering air temperature (RMSE decreased from 5.19 to 5.05 $umol\ CO_2\ m^{-2}\ s^{-1}$, while R^2 values increased from 0.61 to 0.66; Figure S16b).

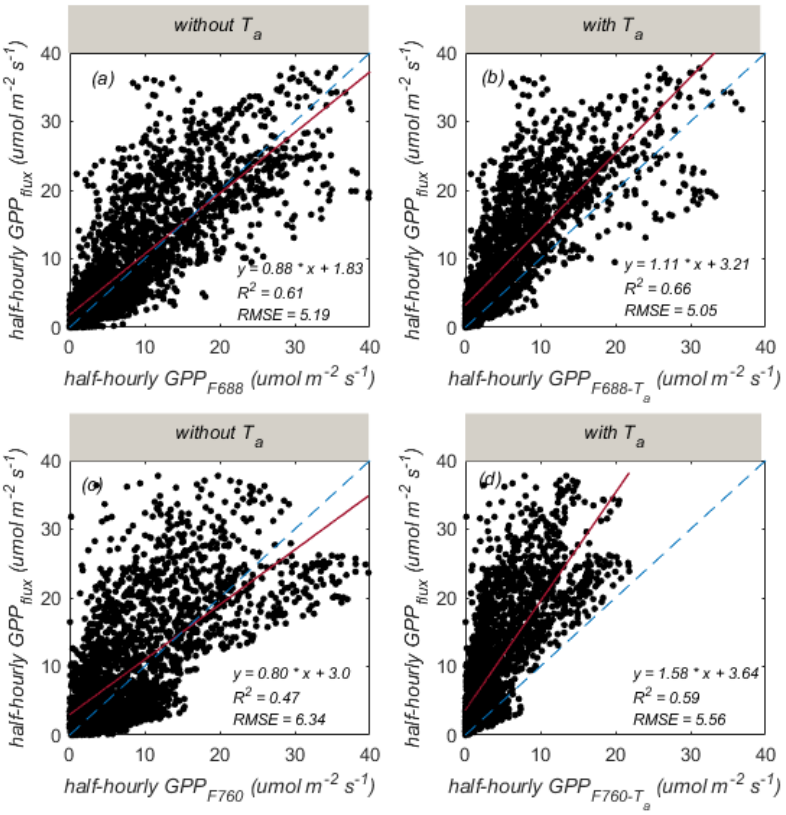

Figure S16. The relationships of GPP with $tSIF_{688}$ (a), $tSIF_{688} * f(Ta)$ (b), $tSIF_{760}$ (c), and $tSIF_{760} * f(Ta)$ (d) based on half-hour measurements. The blue dotted line is the 1:1 line.

By considering the influences of T_a, $tSIF_{760}$-based GPP estimation was improved (RMSE dropped from 5.58 to 4.67 $umol\ CO_2\ m^{-2}\ s^{-1}$, while R^2 values increased from 0.50 to 0.65; Figure S17d). $tSIF_{688}$-GPP estimation was also improved (RMSE decreased from 4.64 to 4.42 $umol\ CO_2\ m^{-2}\ s^{-1}$, while R2 values increased from 0.65 to 0.69; Figure S17b) by integrating T_a

with $tSIF_{688}$. It indicated that considering the effects of temperature could improve the SIF-based GPP estimation at different time scales.

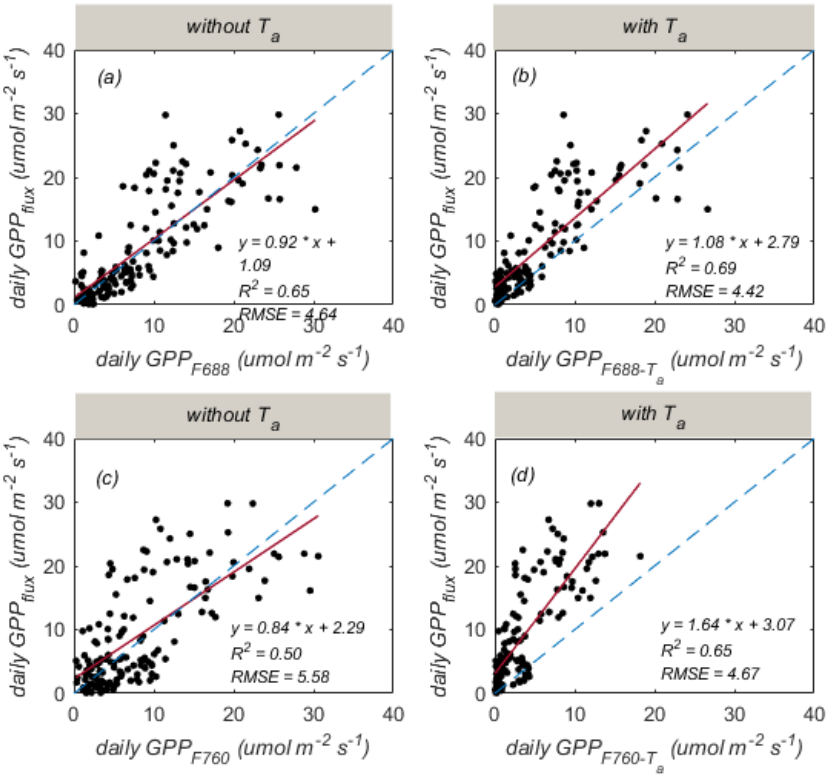

Figure S17. The relationships of GPP with $tSIF_{688}$ (a), $tSIF_{688} * f(Ta)$ (b), $tSIF_{760}$ (c), and $tSIF_{760} * f(Ta)$ (d) based on daily mean data. The blue dotted line is the 1:1 line.

Table S6. The $tSIF$-based GPP models with and without considering the effects of T_a based on half-hourly and daily mean data without the negative $tSIF$ values. The $f(T_a)$ is the temperature-corrected function.

Temporal resolution	Band	Regression Equation	R^2	RMSE
half-hourly	688 nm	$GPP_{F688} = 0.75 \times tSIF_{688}$	0.61	5.19
		$GPP_{F688-T_a} = 0.75 \times f(T_a) \times tSIF_{688}$	0.66	5.05
	760 nm	$GPP_{F760} = 10.58 \times tSIF_{760}$	0.47	6.34
		$GPP_{F760-T_a} = 10.58 \times f(T_a) \times tSIF_{760}$	0.59	5.56
daily	688 nm	$GPP_{F688} = 0.83 \times tSIF_{688}$	0.65	4.64
		$GPP_{F688-T_a} = 0.83 \times f(T_a) \times tSIF_{688}$	0.69	4.42
	760 nm	$GPP_{F760} = 11.8 \times tSIF_{760}$	0.50	5.58
		$GPP_{F760-T_a} = 11.8 \times f(T_a) \times tSIF_{760}$	0.65	4.67

(VII) temperature responses of SIF and GPP during the entire growing period

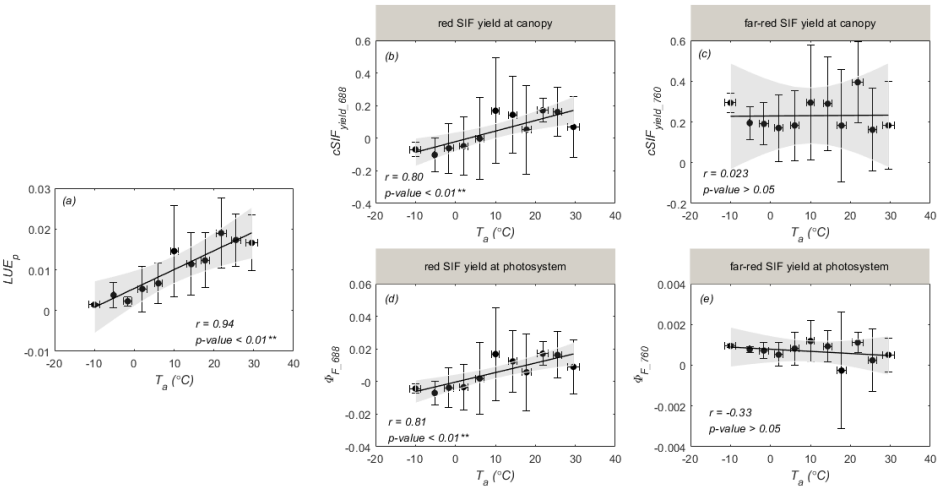

Figure S18. The relationships of daily mean LUE_p (a), $cSIF_{yield\_688}$ (b), $cSIF_{yield\_760}$ (c), Φ_{F_688} (d), and Φ_{F_760} (e) with air temperature (T_a) during the entire growing period. The data were averaged over intervals of 4 ℃, and the error bars indicate the standard deviation. The 95% confidence levels for prediction are represented by the grey-shaded zones.

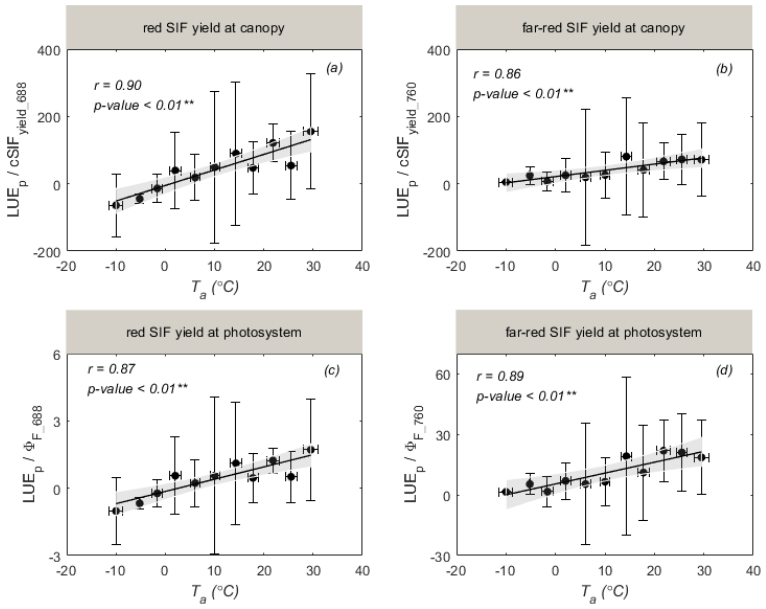

Figure S19. The relationships of daily mean $LUE_p/cSIF_{yield\_688}$ (a), $LUE_p/cSIF_{yield\_760}$ (b), LUE_p/Φ_{F_688} (c), and LUE_p/Φ_{F_760} (d) with air temperature (T_a) during the entire growing period. The data were averaged over intervals of 4 ℃, and the error bars indicate the standard deviation. The 95% confidence levels for prediction are represented by the grey-shaded zones.